RESEARCH ARTICLE

Atmosphere-ocean linkages in the eastern equatorial Pacific over the early Pleistocene

Patricia Povea[1], Isabel Cacho[1], Ana Moreno[2], Leopoldo D. Pena[1,3], Melisa Menéndez[4], Eva Calvo[5], Miquel Canals[1], Rebecca S. Robinson[6], Fernando J. Méndez[7], and Jose-Abel Flores[8]

[1]Grup de Recerca Consolidat en Geociències Marines, Departament de Dinàmica de la Terra i de l'Oceà, Universitat de Barcelona (UB), Barcelona, Spain, [2]Geoenvironmental Processes and Global Change Department, Pyrenean Institute of Ecology-CSIC, Zaragoza, Spain, [3]Lamont-Doherty Earth Observatory, Columbia University, Palisades, New York, USA, [4]Environmental Hydraulics Institute "IH Cantabria", Universidad de Cantabria, Santander, Spain, [5]Institut de Ciències del Mar, Consejo Superior de Investigaciones Científicas (CSIC), Barcelona, Spain, [6]Graduate School of Oceanography, University of Rhode Island, Kingston, Rhode Island, USA, [7]Departamento de Ciencias y Técnicas del Agua y del Medio Ambiente, E.T.S. Ingenieros de Caminos, Universidad de Cantabria, Santander, Spain, [8]Department of Geology, University of Salamanca, Salamanca, Spain

Abstract Here we present a new set of high-resolution early Pleistocene records from the eastern equatorial Pacific (EEP). Sediment composition from Ocean Drilling Program Sites 1240 and 1238 is used to reconstruct past changes in the atmosphere-ocean system. Particularly remarkable is the presence of laminated diatom oozes (LDOs) during glacial periods between 1.85 and 2.25 Ma coinciding with high fluxes of opal and total organic carbon. Relatively low lithic particles (coarse and poorly sorted) and iron fluxes during these glacial periods indicate that the increased diatom productivity did not result from dust-stimulated fertilization events. We argue that glacial fertilization occurred through the advection of nutrient-rich waters from the Southern Ocean. In contrast, glacial periods after 1.85 Ma are characterized by enhanced dust transport of finer lithic particles acting as a new source of nutrients in the EEP. The benthic ecosystem shows dissimilar responses to the high productivity recorded during glacial periods before and after 1.85 Ma, which suggests that the transport processes delivering organic matter to the deep sea also changed. Different depositional processes are interpreted to be the result of two distinct glacial positions of the Intertropical Convergence Zone (ITCZ). Before 1.85 Ma, the ITCZ was above the equator, with weak local winds and enhanced wet deposition of dust. After 1.85 Ma, the glacial ITCZ was displaced northward, thus bringing stronger winds and stimulating upwelling in the EEP. The glacial period at 1.65 Ma with the most intense LDOs supports a rapid southward migration of the ITCZ comparable to those glacial periods before 1.85 Ma.

1. Introduction

The Early Pleistocene climate evolution is marked by the progressive strengthening of the Northern Hemisphere glaciation (NHG), and it has been argued that this situation strengthened trade winds, inducing a cooling in tropical sea surface temperatures (SSTs) by enhanced upwelling activity [*Marlow et al.*, 2000]. Meanwhile, land records indicate an enhanced aridity along the tropical belt with consequences on African faunal evolution [*deMenocal*, 1995, 2004; *Feakins et al.*, 2005; *Trauth et al.*, 2007]. The obliquity imprint upon tropical proxy records further supports the high-latitude control over tropical regions during this period [*Liu and Herbert*, 2004; *Herbert et al.*, 2010].

The eastern equatorial Pacific (EEP) is known by its highly productive upwelling system, which has operated with varying intensity across glacial-interglacial cycles [*Lyle et al.*, 1988; *Weber and Pisias*, 1999; *Murray et al.*, 2000]. During the early Pleistocene, 400 kyr eccentricity cycles seem to have ultimately controlled major changes of SST in the EEP, with abrupt and intense cooling events at 1.7 and 2.1 Ma [*Herbert et al.*, 2010].

Nevertheless, several records from the EEP reveal a rather complex link between SST and primary productivity across the Pleistocene [*Dekens et al.*, 2007; *Lawrence et al.*, 2006; *Ma et al.*, 2015]. In particular, a remarkable period of enhanced EEP primary productivity between 1.6 and 2.9 Ma was reflected in unusually high-alkenone concentrations [*Lawrence et al.*, 2006] without any clear expression of colder SST. Such signal decoupling has been attributed to EEP fertilization due to an increase in nutrient availability finally driven by changes in nutrient utilization in the Southern Ocean [*Lawrence et al.*, 2006; *Etourneau et al.*, 2013]. Nitrogen isotopes support a sharp increase in EEP denitrification but starting later, after 2.1 Ma, which is attributed to an enhanced upwelling activity due to strengthened Walker circulation [*Liu et al.*, 2008]. This situation is consistent with a
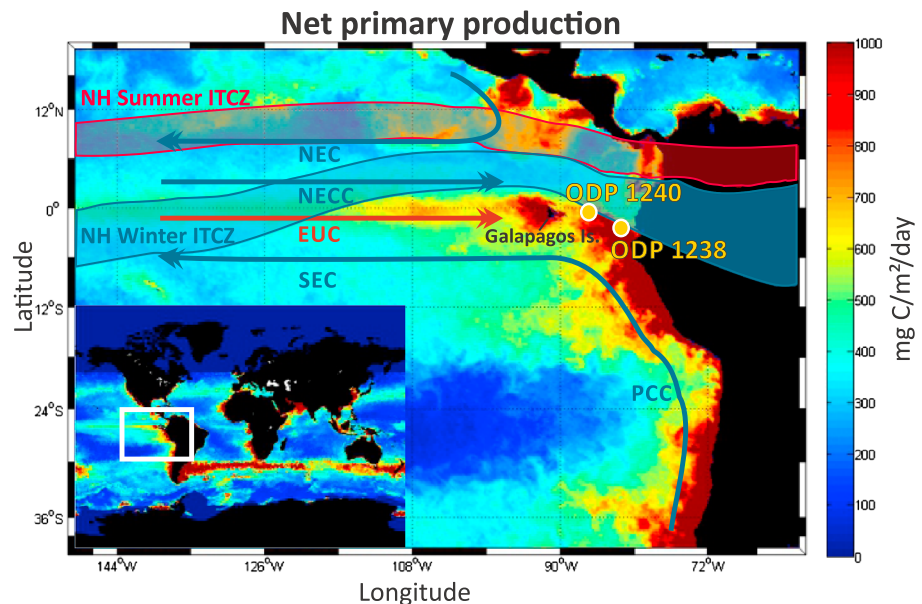
Figure 1. Regional oceanography and net primary production (NPP) from the eastern equatorial Pacific (EEP). Surface and subsurface currents in the EEP, Equatorial Undercurrent (EUC), North Equatorial Current (NEC), North Equatorial Countercurrent (NECC), Peru-Chile Current (PCC), and South Equatorial Current (SEC). NPP in the surface waters of modern EEP is based on the standard VGPM algorithm [*Behrenfeld and Falkowski*, 1997]. Data were downloaded from the Ocean Productivity site. Northern Hemisphere summer and winter positions of the ITCZ have been marked with blue and red bands. ODP Sites 1240 and 1238 are labeled with yellow dots.

major atmospheric reorganization including an intensification of the Walker circulation and the onset of a strong equatorial west-east gradient at 1.5–2 Ma, as indicated by SST and isotopic records from both western equatorial Pacific (WEP) and EEP [*Ravelo et al.*, 2004; *Wara et al.*, 2005; *Etourneau et al.*, 2010; *Ravelo et al.*, 2014]. This time period also appears to be critical in Southern Atlantic Ocean where a reinforcement of trade winds and the strengthening of the associated upwelling have been noticed [*Etourneau et al.*, 2009].

Nevertheless, this atmospheric reorganization has been questioned by new long multiproxy records that suggest a relatively constant E-W equatorial Pacific SST gradient since the Pliocene and, consequently, an essentially rather constant and continuously active EEP upwelling system [e.g., *Zhang et al.*, 2014; *O'Brien et al.*, 2014]. The debate is far from being settled [*Ravelo et al.*, 2004; *Wara et al.*, 2005; *Ravelo et al.*, 2014].

Thus, several records support the occurrence of EEP productivity and atmospheric changes during the early Pleistocene, but their occurrence is not always apparently synchronous and their coupling is still puzzling. The lithic fraction of deep-sea sediments is a proxy that could shed light on atmospheric changes in the EEP. It has been used to track the location of the Intertropical Convergence Zone (ITCZ), which would have migrated southward from the late Miocene to present [*Hovan*, 1995; *Hyeong et al.*, 2006]. Unfortunately, these studies lack the temporal resolution to evaluate rapid changes that might have occurred during the early Pleistocene. Short-term reconstructions of changes in the average ITCZ location have concentrated on glacial-interglacial cycles of the late Pleistocene and Holocene and are mostly based on SST marine records, humidity terrestrial records, or model assimilations [*Koutavas and Lynch-Stieglitz*, 2004; *Peterson and Haug*, 2006; *Broccoli et al.*, 2006; *McGee et al.*, 2014; *Schneider et al.*, 2014].

Elucidating the link between any early Pleistocene atmospheric reorganization and productivity changes in the EEP upwelling requires using parallel records of proxies sensitive to both atmospheric and marine conditions. In this paper we present a novel very high resolution multiproxy study over the 1.56–2.26 Ma time interval in the EEP, resulting from the detailed analysis of biogenic and lithogenic components in deep-sea sediments. The study focuses on Ocean Drilling Program (ODP) Site 1240, located at the northern edge of the equatorial cold water tongue (Figure 1) and thus, made this site potentially sensitive to changes in the atmospheric-ocean coupled system [*Hovan*, 1995; *Mix et al.*, 2003]. Previous results for this ODP site have shown major changes in the sediment composition occurring along the early Pleistocene, which were linked to shifts in the regional

atmosphere-ocean system [*Mix et al.*, 2003]. Moreover, ODP Site 1240 contains sequences of laminated diatom oozes (LDOs), which become a valuable paleoproductivity indicator. In order to ground truth our results and achieve a broader evaluate the geographical extension, the data obtained from ODP Site 1240 have been compared with data from ODP Site 1238, located further south and closer to the South American coastline. Thus, this study offers an exceptional time resolution for the early Pleistocene and demonstrates that the observed changes occurred as rapid transitions related to glacial-interglacial cycles, rather than as progressive long-term change.

2. Oceanographic and Atmospheric Setting

The EEP is one of the most productive upwelling areas in the world controlled by the trade wind systems [*Chelton et al.*, 2001]. This atmospheric convergence near the equator and the ascending branch of the Hadley cell define the position of the ITCZ and control the surface ocean properties [*Koutavas and Lynch-Stieglitz*, 2004]. Surface ocean circulation in the EEP is characterized by the north-south asymmetry of the surface currents, as a consequence of the trade winds intensity [*Wyrtki*, 1974]. ODP Sites 1240 and ODP 1238 locations are both influenced by the South Equatorial Current (SEC), which is the continuation of the Peru-Chile Current (PCC), centered at about 5°S under the southeast trade winds [*Wyrtki*, 1967; *Kessler*, 2006]. During the Southern Hemisphere winter, when SE trade winds are strengthened, the SEC is more intense [*Wyrtki*, 1967]. In the subsurface, the Equatorial Undercurrent (EUC) flows eastward along the equator, and replaces surface water driven westward by the trades [*Kessler*, 2006], providing nutrients to the EEP that are sourced in the polar regions, mainly from the Southern Ocean [*Calvo et al.*, 2011; *Sarmiento et al.*, 2004; *Pena et al.*, 2013] (Figure 1). Recent studies suggest that Galapagos Islands could influence the flow of EUC east of 95°W, acting as a topographic barrier, although its influence has not been fully characterized yet [*Karnauskas et al.*, 2007, 2010].

The strong southeasterly winds that cross the equator induce an Ekman divergence zone, which allows the upwelling of nutrient-rich and cold waters from the EUC, particularly during the Southern Hemisphere winter (Figure 1) [*Wyrtki*, 1981]. The extent of the cold tongue created by the upwelling is limited by the equatorial front (EF), the position of which varies seasonally. The EF reaches its most northerly position during the Northern Hemisphere summer [*Pak and Zaneveld*, 1974; *de Szoeke et al.*, 2007]. In the modern EEP, biological activity does not consume all the macronutrients upwelled to the surface due to limitations in the supply of iron and silicic acid [*Brzezinski et al.*, 2008]. Iron is a micronutrient that limits macronutrient utilization, and thus, it can ultimately control the primary production of the upwelling system [*Jickells et al.*, 2005; *Mahowald et al.*, 2005]. Since the EUC is typically iron depleted by the time it reaches the EEP [*Kaupp et al.*, 2011], the main iron contribution occurs through eolian dust deposition. This induces a strong connection between dust fluxes, iron input, and primary productivity in the EEP [*Martin*, 1990; *Jickells et al.*, 2005].

At present, the mean ITCZ position is shifted toward the Northern Hemisphere as a consequence of a northward heat transport across the equator by ocean circulation [*Marshall et al.*, 2014]. ITCZ migrations can also be the result of changes in the interhemispheric temperature contrast [*Broccoli et al.*, 2006], responding to seasonal changes in insolation and atmosphere-ocean interactions [*Xie and Philander*, 1994]. During Northern Hemisphere summer, when the southeasterly trades are stronger [*Chelton et al.*, 2001; *Koutavas and Lynch-Stieglitz*, 2004], the ITCZ is positioned at about 10°N and both maximum upwelling and significant eolian deposition of dust from South America occur in the EEP [*Molina-Cruz*, 1977]. The ITCZ migrates southward when the southeasterly trades are weaker [*Chelton et al.*, 2001], between February and April, reducing the dust input and weakening upwelling. Paleoclimate records and numerical models suggest that the southward migration may have been greater during colder phases of the Northern Hemisphere on a variety of time scales, such as the Little Ice Age (LIA), shifting the ITCZ well south of its most southern present position [*Koutavas and Lynch-Stieglitz*, 2004; *Chiang and Bitz*, 2005; *Broccoli et al.*, 2006; *Sachs et al.*, 2009].

3. Materials and Methods

ODP Site 1240 (0°01.31′N, 86° 27.76′W; 2921 m water depth) and ODP Site 1238 (1°52.310′S, 82°46.934′W; 2203 m water depth) were retrieved in the EEP, from the northern and southern flank of the Carnegie Ridge, respectively, in the Panama Basin during the ODP Leg 202, by *JOIDES Resolution* in 2002 (Figure 1) [*Mix et al.*, 2003].

The recovered sedimentary sequence of ODP Site 1240 is a fossil-rich mud with variable composition [*Mix et al.*, 2003]. Three subunits (1A, 1B, and 1C) were defined according to their dominant sedimentological characteristics
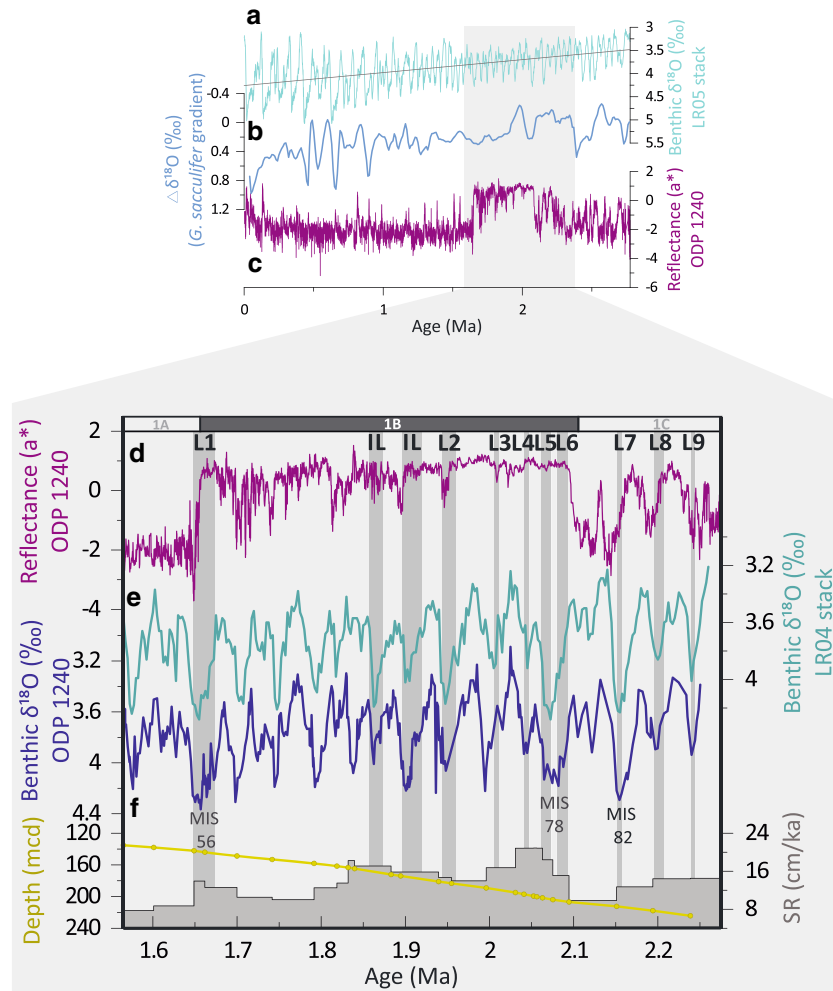
Figure 2. Chronological framework for ODP Site 1240. (a) Global benthic $\delta^{18}O$ stack (LR04 stack) [*Lisiecki and Raymo*, 2005]. (b) Oxygen isotope difference (*Globigerinoides sacculifer*) between ODP Site 851 (Eastern Pacific) [*Cannariato and Ravelo*, 1997] and ODP Site 806 (Western Pacific) [*Berger et al.*, 1993; *Jansen et al.*, 1993]. (c) ODP Site 1240 reflectance (a*) for the last 2.7 Ma [*Blum et al.*, 2005] shows abrupt variations in sediment composition for the studied interval. (d) ODP Site 1240 reflectance (a*) for the studied period [*Blum et al.*, 2005], showing three subunits clearly marked and represented as a white and gray bar (1A, 1B, and 1C). (e) Age model from ODP Site 1240, developed by comparison of high-resolution ODP Site 1240 benthic $\delta^{18}O$ and global benthic $\delta^{18}O$ stack. (f) Tie points and linear sedimentation rates from ODP Site 1240 for the studied interval. The gray shaded vertical bars indicate the position of the observed and the interpreted LDOs, labeled as L1–L9 and IL, respectively. Marine isotopic stages (MISs) 56, 78, and 82 are also shown.

[*Mix et al.*, 2003]. In this work we focus on subunit 1B, in the depth interval from 135.34 to 225.94 meters composite depth (mcd), between 1.65 and 2.1 Ma, which presents higher reflectance (a*) values (Figure 2). It was initially proposed to reflect an intensification of atmospheric circulation, based on the preliminary results of grain density, biogenic silica, total organic carbon (TOC) content, and the shipboard stratigraphic description presented in *Mix et al.* [2003]. Eleven LDOs were described mainly within subunit 1B (1.65–2.2 Ma) [*Mix et al.*, 2003] (see section 5.1). They are composed largely of pennate diatoms, such as *Thalassiothrix* spp., that tend to form large grids of strongly intertwined cells.

The sedimentary sequence from ODP Site 1238 is mostly formed by diatom nannofossil ooze and bioturbated nannofossil oozes with a variable abundance of clay and foraminifera [*Mix et al.*, 2003]. The analyzed sequence is centered from 79 to 99 mcd, in interval of 1.6–1.75 Ma.

3.1. Oxygen Isotope Record

In order to establish robust chronology, we measured benthic foraminifer $\delta^{18}O$ from ODP Site 1240, which was based in the analysis of two different species of benthic foraminifera, *Uvigerina* spp. and *Cibicidoides wuellerstorfi*.

Each measurement of *Uvigerina* spp. was made on eight to ten individuals. Measurements of *C. wuellerstorfi* were performed on four to five individuals ($>212\,\mu$m). Samples were crushed to open the foraminiferal chambers and then cleaned with reagent grade methanol in order to remove attached clay particles. All measurements were made with a Finnigan-MAT252 mass spectrometer fitted with a Kiel Carbonate Device I in the Scientific and Technological Center of the University of Barcelona (CCiT-UB). Values are reported as per mille with respect to the Vienna Peedee belemnite standard. For the duration of the analyses, external reproducibility was always better than 0.06‰ for δ^{18}O. In order to produce the composite δ^{18}O record, the *C. wuellerstorfi* results were corrected to the *Uvigerina* scale by adding 0.64‰ [*Shackleton and Hall*, 1984].

3.2. Biogenic Fraction: Total Organic Carbon, Nitrogen Content, Opal Content, and *Uvigerina* spp. Abundance

EEP biogenic fractions (TOC, total nitrogen (TN), opal, and *Uvigerina* spp. abundance) were analyzed to monitor past changes in the ocean productivity system. TOC and total nitrogen (TN) content were analyzed at the CCiT-UB using an elemental organic analyzer Thermo EA Flash 1112. TOC was measured in 25% HCl-treated sediment samples [*Fabres et al.*, 2002].

Biogenic silica concentrations were measured in 200 mg samples of bulk sediment. The extraction method is modified from *Povea et al.* [2015] and includes a two-step leaching with a 1.5 M NaOH solution. Si concentration in both leachates was determined through inductively coupled plasma optic spectrometer (ICP-OES), using a PerkinElmer model Optima 3200 RL at the CCiT-UB. Biogenic opal concentrations were determined from Si concentrations multiplying the obtained values by 2.4 [*Mortlock and Froelich*, 1989].

The main benthic foraminifera genera present in the samples were counted to identify any major change in the assemblage, which could be indicative of changes in the deep ocean nutrient content and oxygen concentration. The principal benthic foraminiferal assemblage is formed by *Giroydina* spp., *Uvigerina* spp., *Melonis* spp., *Cibicides wuellerstorfi*, and *Cibicides kullenbergi* in order of abundance. After a preliminary low-resolution counting (107 samples with a 6.5 kyr average time resolution) considering these five genera, *Uvigerina* spp. was selected to generate high-resolution counts over the whole sequence because it showed the greatest variability.

3.3. XRF Core Scanner Measurements

XRF core scanner was used in order to achieve at high resolution the elemental composition of the EEP sediments. Sampling for XRF core scanner analyses was done at the Gulf Coast ODP repository at Texas. U-channels were collected by pushing rigid u-shaped plastic liners (2×2 cm cross section, 1.5 m in length) into the core sections to collect narrow continuous samples of core. XRF core scanner analyses were done at the University of Bremen (Germany). The XRF analyzes the very top of the sediment surface over 1 cm^2 area, using 30 s count time, 20 kV X-ray voltage, and an X-ray current of 0.087 mA to obtain statistically significant Fe counts. A detailed description of the applied X-ray fluorescence analysis and the system configuration of the XRF core scanner at the University of Bremen are given in *Jansen et al.* [1998] and *Röhl and Abrams* [2000]. The resulting data represent element intensities in counts per second, and all the intensities are above the detection limits [*Richter et al.*, 2006]. Intensity values were converted to concentrations through calibration with absolute elemental concentrations obtained from 30 sediment samples selected along this section (see section 5.5). Sediment samples were analyzed by ICP-OES at the CCiT-UB after total digestion of 50 mg of dried bulk sediment material in a pressure digestion system with a mixture of 3 mL HNO$_3$ 65%, 2 mL HF 40%, and 2 mL HCl 32%. After decomposition, the samples were heated to dryness, redissolved in 5 mL of 6.5% HNO$_3$, and homogenized in the microwave. Fe element was analyzed by ICP-OES in a PerkinElmer Optima 3300 RL with a precision better than 2%. The accuracy of element determinations was checked using standard reference materials. The ICP-OES obtained values were used to transform the XRF data into concentration values (mg/g). Correlation equations with $r^2 = 0.79$ indicate a high correlation between both methods, thus allowing the data conversion (Figure S1 in the supporting information).

3.4. Grain Size and Mineralogical Analyses

Grain size analysis and mineralogical description have been conducted to characterize the lithic fraction that reached the eastern equatorial Pacific. Prior to the grain size analysis, samples were processed with a protocol specifically designed to ensure the complete removal of all the biogenic (organic matter, carbonate, and biogenic silica) and authigenic components (diagenetic oxides), leaving only the lithogenic components [*Povea et al.*, 2015]. After this procedure, smear slides were prepared for each sample using a UV curing adhesive

and dried under an ultraviolet light [*Backman and Shackleton*, 1983; *Rothwell*, 1989]. They were then observed with a microscope to ensure the quality of the procedure as well as to determine the percentages of the main mineralogical components of the lithic fraction [*Povea et al.*, 2015]. Mineral abundance was estimated using the comparison chart for visual percentage estimation [*Terry and Chilingar*, 1955]. Grain size distributions were determined using a Coulter LS 230 on the lithic fraction. In addition, the lithic percentage was calculated for the studied interval (1.56–2.26 Ma). Bulk dry samples were weighed before the removal of the biogenic fraction. After the application of the biogenic removal procedure, the samples were lyophilized and weighed. The difference between these weights gives the biogenic fraction removed. Thus, the lithic percentage was obtained after subtracting the biogenic percentage from the total percentage (lithic percentage = 100% − % biogenic fraction).To aid in the interpretation of the large grain size data set, a statistical method using a k-means clustering algorithm was applied [*Povea et al.*, 2015]. This method divides the data set into *n* clusters, which are represented by its centroid and formed by the data for which the centroid is the nearest [*Hastie et al.*, 2001]. The degree of representation of each cluster in each sample is obtained by calculating the Euclidean distances between each cluster centroid and the *N* data.

4. Chronological Framework

The age model is based on visual alignment of the high-resolution benthic δ^{18}O isotopic record from ODP Site 1240 with the LR04 stack [*Lisiecki and Raymo*, 2005], including tie points every ~27 kyr on average ($r^2 = 0.76$; Figure 2). Our sequence corresponds to the time interval between 1.56 and 2.26 Ma, comprising the early Pleistocene from marine isotopic stage (MIS) 52 to MIS 86. Sedimentation rates vary through this interval, with values oscillating between 7.7 and 20.9 cm/ka. These sedimentation rates are relatively high for this area and can be attributed both to the high particle flux from the equatorial upwelling system and to the basin morphology, an abyssal valley which acts as natural sediment trap [*Mix et al.*, 2003]. The studied interval provides a time resolution of 4 kyr on average for the lithic and biogenic records and 170 years for the XRF scanner data.

Mass accumulation rates for the biogenic and lithic records were calculated based on linear sedimentation rates and dry bulk density (DBD). This density has been estimated from a linear correlation ($r^2 = 0.92$) between gamma ray attenuation bulk density and the available DBD discrete measurements (Figure S2 in the supporting information) [*Mix et al.*, 2003].

5. Results

5.1. Laminated Diatom Oozes

Lithology from ODP Site 1240 is mostly dominated by diatom-nannofossil ooze or diatom-bearing nannofossil ooze. The identification of the laminated diatom oozes is based on the visual identification of centimeter-thick color bands from dark olive to olive and dark olive brown. In contrast, the sediment color in the nonlaminated intervals alternates between pale olive and light olive gray and presents frequent bioturbation marks of *Zoophycos* burrowing [*Mix et al.*, 2003]. Diatom assemblage during the laminated layers is dominated by *Thalassiothrix* spp. and *Thalassionema* spp., while the nonlaminated layers are dominated by *Azpeitia nodulifera* (Figure S3 in the supporting information). The observed LDOs (labeled as L1 to L9) have been defined based on the visual identification due the dark olive brown color. The interpreted LDOs (labeled as IL) have been determined since exhibiting the same pattern of the observed LDOs, based on the highest concentrations of biogenic silica and lithic contents, albeit its visual identification is not so clear.

5.2. Oxygen Isotope Record

The benthic δ^{18}O record has values that range from 3.2 to 4.5‰ with oscillations corresponding to glacial/interglacial cycles (Figure 2). The data reveal very sharp transitions between interglacial and glacial phases. Three remarkable glacial periods are recorded as presenting the highest δ^{18}O values and the longest durations, MIS 56 (1.65–1.67 Ma), MIS 78 (2.07–2.09 Ma), and MIS 82 (2.15–2.17 Ma).

5.3. Grain Size Distribution and Clustering Analysis

Particle size distributions reveal that most of samples are trimodal, with one initial mode around 0.5 μm, followed by a principal mode centered at 6–7 μm. After this principal mode, a high variability of grain size modes is observed between 100 and 400 μm (Figure 3). However, in certain time intervals, mainly before 1.85 Ma, the main mode is displaced to coarser grains (>60 μm) and the samples are overall poorly sorted.
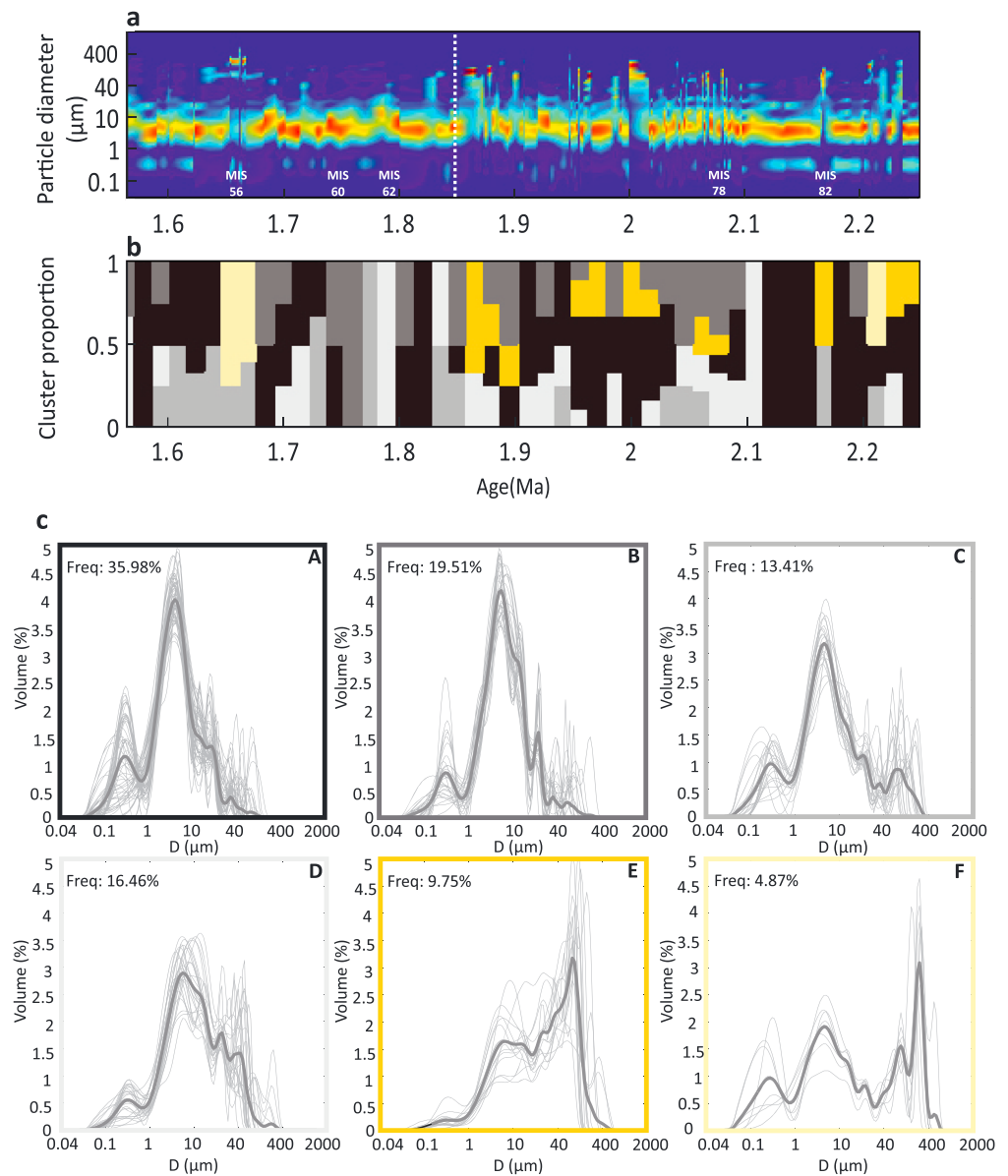
Figure 3. Clustering analysis of ODP Site 1240 particle size distribution. (a) Particle size distribution of the entire studied period. (b) Proportion and distribution of six clusters along the studied period; note that each color corresponds to each cluster of the next caption. (c) Cluster classification based on their particle size distribution [*Povea et al.*, 2015]. Frequency distribution is noted for each cluster. Marine isotopic stages (MISs) 56, 60, 62, 78, and 82 are also shown.

According to the obtained modal distribution, *k-means* clustering analysis characterizes the grain size data set into six clusters (cluster A to cluster F), previously presented in *Povea et al.* [2015]. Clusters A, B, and C are the most dominant patterns, reaching almost 69% of the frequency (Figure 3c). These clusters show a well-defined main mode around 6–7 μm, a finer mode around 0.5 μm, and a more variable last mode. Clusters E and F are less abundant, with a combined frequency of 15%, and clearly different from the rest, presenting a main mode shifted to coarser sizes (Figure 3c). Cluster D seems to be the intermediate and transitional pattern between the well-sorted (clusters A, B, and C) and the poorly sorted and coarser (clusters E and F) clusters (Figure 3c), with the mode around 6–7 μm less defined and a terminal mode more abundant.

In order to better understand the time distribution of these distinct clusters, cluster E distance is estimated. This value reflects the degree of similarity between each sample and this cluster, where the lower value (close to 0) means the greater similarity to cluster E. Cluster E has been chosen for its most distinct modal distribution,
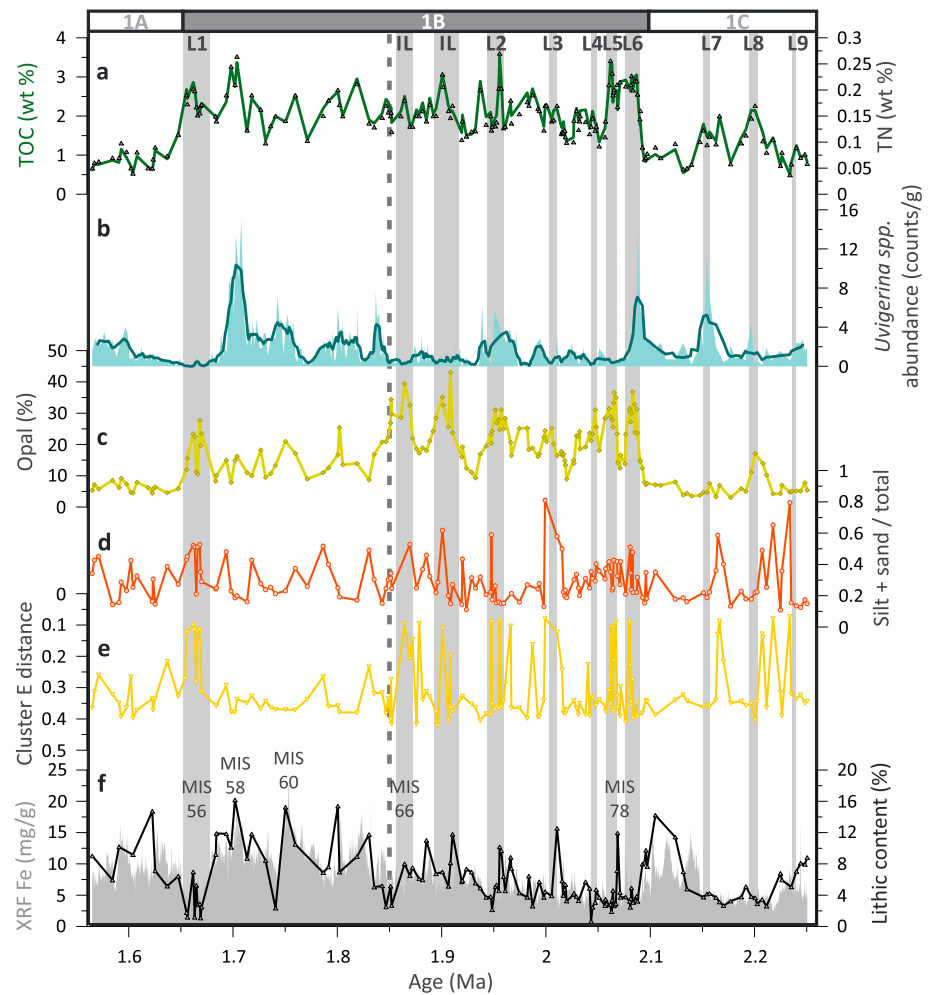
Figure 4. Biogenic and lithogenic fraction characterization from eastern equatorial Pacific (ODP Site 1240). (a) TOC (solid line) and TN (gray triangles) contents (%). (b) *Uvigerina* spp. abundance (counts/g); note that the green dark line shows the running average of five points. (c) Opal (%). (d) Grain size parameter shown as (silt + sand)/total. (e) Euclidean distance of cluster E to each sample. (f) XRF core scanner Fe (mg/g) and lithic content (%). The gray shaded vertical bars indicate the position of the observed and the interpreted LDOs, labeled as L1–L9 and IL, respectively. The white and gray bar on the top shows the three sedimentological units (1A, 1B, and 1C). The vertical dashed line marks the 1.85 Ma transition. Marine isotopic stages (MISs) 56, 58, 60, 66, and 78 are also presented.

displaying a coarser main mode, and its frequent presence during colder phases, especially during LDO deposition (Figure 4e). The comparison with the abundance of the coarse fraction represented by the silt + sand/total ratio (Figure 4d) shows a generally good agreement between these two parameters that both peak during glacial periods. However, cluster E practically disappears during glacial times without LDOs. While the silt-clay parameter does not differentiate between these two groups of glacial periods, the absence of cluster E indicates that the lithic fraction during the non-LDO glacial phases had a distribution closer to A, B, C, and D clusters (e.g., MIS 58 and MIS 60 in Figures 3 and 4).

5.4. Paleoproductivity Proxies

TOC and TN records show substantial variability over the studied time interval, with generally higher values during the glacial intervals when LDOs occurred (Figure 4a). These records exhibit three distinct intervals, consistent with previously defined subunits [*Mix et al.*, 2003], with higher TOC and TN mean values during subunit 1B (Table 1) and very sharp boundaries between subunits. The upper part (1.56–1.65 Ma) presents the minimum values of all the sequence, while the middle interval (1.65–2.09 Ma) shows the maximum values of TOC, TN, and opal (Table 1). The biogenic fluxes of TOC and opal also show the highest values during subunit 1B (Figures 5e and 5g), with maximum values during the LDO intervals.

Table 1. Biogenic Contents From Eastern Equatorial Pacific (TOC, TN, and Opal)[a]

Record (wt %)	Unit 1A			Unit 1B			Unit 1C		
	Minimum	Maximum	Average	Minimum	Maximum	Average	Minimum	Maximum	Average
TOC	0.5	1.5	0.86	0.84	3.5	2.16	0.5	2.15	1.2
TN	0.04	0.11	0.069	0.06	0.27	0.15	0.03	0.17	0.09
Opal	4.41	9.19	6.24	7.81	43.03	21.12	3.02	17.10	6.51

[a]Divided in the three sedimentological subunits (1A, 1B, and 1C).

Uvigerina spp. abundance oscillates from 0 to 80% of the total benthic assemblage (Figure 4b). High *Uvigerina* spp. abundances typically occur in phases of relatively high TOC percentages with some exceptions, when peaks in TOC% correspond to low *Uvigerina* spp. abundance, and these events mostly correspond to the LDOs (Figures 4a and 4b).

5.5. Lithic Fraction and Iron

The record of lithic percentage mimics, at lower resolution, the iron content profile measured by the XRF scanner for the whole studied period (Figure 4f). This relationship ($r^2 = 0.63$), together with the absence of fluvial runoff to the studied basin, supports their common origin and thus the eolian deposition of the measured iron. In contrast to the biogenic proxies, these terrigenous source proxies do not differentiate the three sediment subunits (Figure 4f) but show a general increasing trend toward the top of the studied period also shown in the lithic and iron fluxes (Figures 4f, 5j, and 5k and Figure S5 in the supporting information). Interestingly, the higher values occurred during the glacial periods between 1.68 and 1.85 Ma, when the cluster E and silt + sand/total parameter did not agree. On the contrary, the minimum values occurred during the glacial periods previous to 1.85 Ma when cluster E was better represented. The pronounced minimum in both iron and terrestrial content associated with MIS 56, corresponding to the last and very pronounced LDOs (L1).

The mineralogical composition of the lithic fraction is dominated by six main mineral phases that remain constant in composition over the studied period (1.56–2.26 Ma; Figure S6 and Table S1 in the supporting information). The most abundant phases are feldspar (42.15%), opaques (25.45%), and quartz (19.43%), and the minor mineral components are epidote (6.50%), volcanic glass (4.52%), and amphibole (1.95%).

6. Discussion

6.1. Changes in Atmospheric Transport

Since terrigenous sediment comes to the studied location primarily through the atmosphere, its characteristics should reflect the ITCZ position and intensity of the wind belt system, as well as changes in the aridity of the source area. Previous studies have found that eolian dust in the EEP comes from the arid areas of western South America [*Nakai et al.*, 1993], mostly from the Atacama desert [*Molina-Cruz*, 1977] or from the Andean region [*Janecek and Rea*, 1985; *Chuey et al.*, 1987; *Rea*, 1990]. Moreover, Atacama desert became hyperarid in the Pliocene as a consequence of a global climate cooling [*Hartley and Chong*, 2002]. This episode of hyperaridity produced a sedimentary hiatus in the Atacama region from 3.37 Ma, which would be coeval to a major development of Antarctica ice sheets and to an enhancement of the cold ocean upwelling in the eastern Pacific during the Pliocene-Pleistocene transition [*Sáez et al.*, 2012]. Thus, these cooling stages could trigger the extreme hyperarid conditions in the Atacama region with an absence of sediment production and accumulation [*Sáez et al.*, 2012].

Deposition of lithic material, including iron, was relatively low during the time interval prior to 1.85 Ma (Figures 5j and 5k). During this period, the grain size distribution results at Site 1240 show the dominance of giant (>60 μm) and relatively poorly sorted coarse grains (Figure 3c, clusters E and F). In some extreme cases, within the period previous to 1.85 Ma, the fine dominant mode between 4 and 6 μm completely disappears or become very scarce. These are the samples represented by a low cluster E distance, which means a higher similarity with this cluster (Figure 5h), and happen particularly during glacial periods and coinciding with LDOs and also during the strong event at MIS 56. In contrast, after 1.85 Ma, the samples displayed a characteristic trimodal distribution with a principal mode between 6 and 7 μm, indicating the dominance of better sorted fine grains and low variance, particularly during the glacial times (MISs 58, 60 and 62; Figures 3a, 5j and 5k 60 and 62; Figure 3a). These glacial intervals also record an increased arrival of lithic grains and iron.
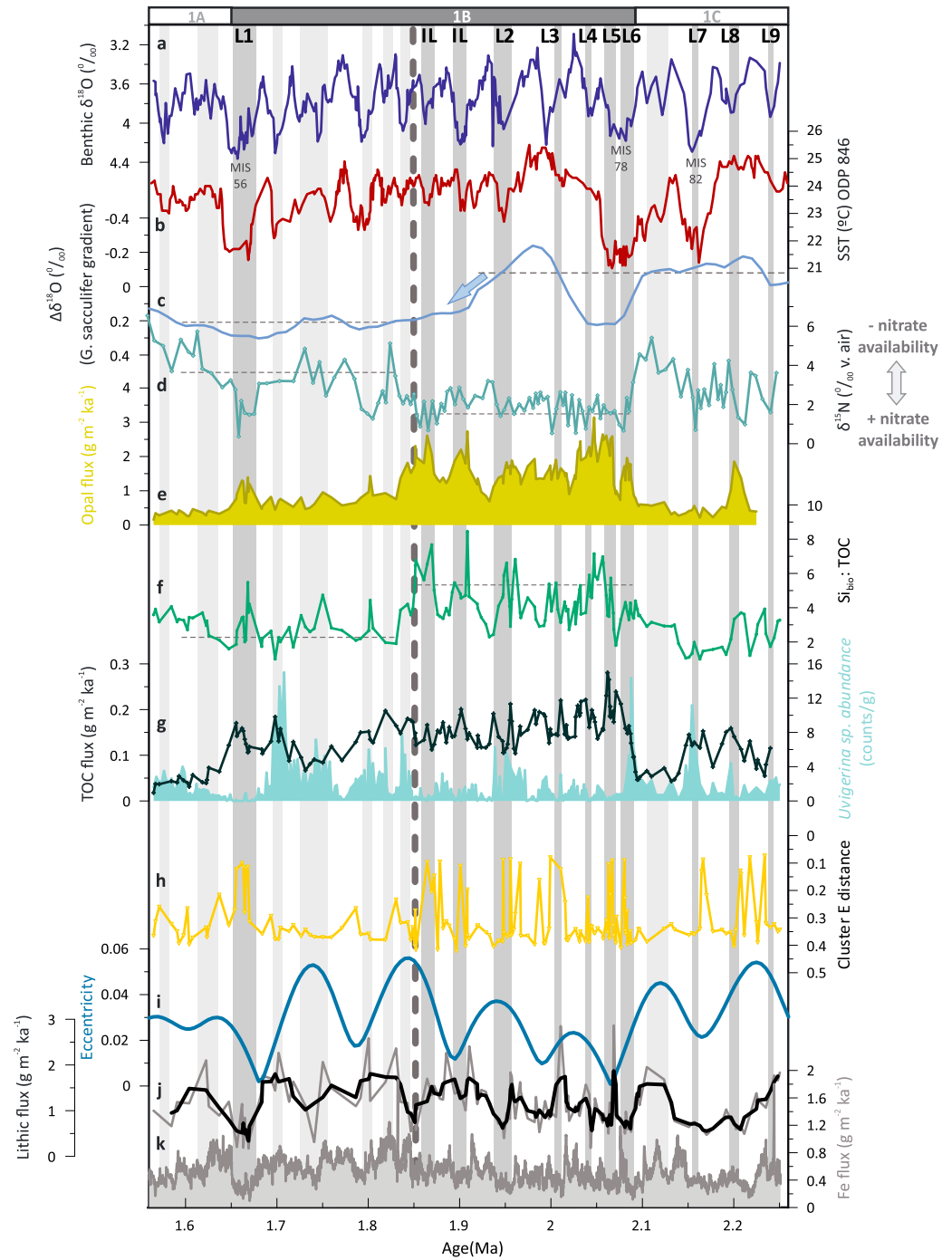
Figure 5. Interpreted ITCZ migrations and distinctive fertilization mechanisms associated to atmosphere-ocean connections over the eastern equatorial Pacific during the studied period. (a) Benthic δ^{18}O record ($^0/_{oo}$). (b) SST (°C) ODP Site 846 [*Herbert et al.*, 2010]. (c) Oxygen isotope difference (*G. sacculifer*) between ODP Site 851 (eastern Pacific) [*Cannariato and Ravelo*, 1997] and ODP Site 806 (western Pacific) [*Berger et al.*, 1993; *Jansen et al.*, 1993]. (d) δ^{15}N ($^0/_{oo}$ v/air) [*Etourneau et al.*, 2013]. (e) Opal flux (gm^{-2} ka^{-1}). (f) Si$_{bio}$/TOC ratio. (g) TOC flux (gm^{-2} ka^{-1}) and *Uvigerina* spp. abundance (expressed as counts/grams dry bulk weight). (h) Cluster E distance. (i) Eccentricity [*Laskar et al.*, 2004]. (j) Lithic flux (gm^{-2} ka^{-1}). (k) Fe flux (gm^{-2} ka^{-1}). The dark gray shaded bars indicate the position of the observed and interpreted glacial LDOs, labeled as L1–L9 and IL, respectively. The light gray shaded vertical bars indicate the glacial periods without LDOs. The white and gray bar on the top shows the three sedimentological units (1A, 1B, and 1C). The vertical dashed line marks the 1.85 Ma transition. Marine isotopic stages (MISs) 56, 78, and 82 are also shown.

The size of dust particles transported over hundreds of kilometers is generally below 10 μm [*Tegen et al.*, 1996]. However, the presence of eolian giant particles (>10 μm) has also been documented in previous studies [*Glaccum and Prospero*, 1980; *Betzer et al.*, 1988; *Moreno et al.*, 2001; *Jeong et al.*, 2013]. These particles can be transported over long distances if strong upward advection of air masses lifts these dust particles to higher altitudes [*Windom*, 1985; *Pye*, 1995] or a midtropospheric wind belt induces a rapid dust transport [*Jeong et al.*, 2013]. An additional factor controlling grain size distribution is the relative contribution of wet and dry deposition [*Guerzoni et al.*, 1997]. The range of grain size particles of dust deposition by a wet event has been explored through the analysis of a series of Saharan dust samples collected in Iberia during rain events (mean Saharan dust wet deposition; Figure S7 in the supporting information), showing that a wide size range of particles can be transported and deposited but always with a strong presence of the coarser mode.

These observations would suggest that most of the samples result from a mixture of wet and dry deposition processes. Nevertheless, when samples get closer to the cluster E, deposition is dominated by wet deposition, consistent with the proximity to the particle size distribution from the Saharan dust (wet deposition; Figure S7 in the supporting information). These changes in the grain size distribution reflect the position of the ITCZ. Strong southeasterly trade winds occur south of the ITCZ, while within the ITCZ, the trade winds become weaker and wet deposition dominates [*Hovan*, 1995]. Consequently, it appears that during glacial periods with the occurrence of the LDOs, mostly before 1.85 Ma, the ITCZ was located at its southernmost position, just above ODP Site 1240. The presence of coarser grains, even giant particles (>200 μm), and scarcity of lithic and iron contents, indicates the dominance of weak southeasterly winds and increased rainfall or wet deposition events. The lithic fraction presents a coherent trend with eccentricity [*Laskar et al.*, 2004], with minimum values at eccentricity minima (Figures 5i–5k). Low eccentricity in the glacial periods previous to 1.85 Ma would have reduced seasonal contrast, and thus ITCZ seasonal migration, anchoring it in a southerly position. This is particularly evident in glacial stages MIS 78 and 56 when intense and long glacial conditions are observed, highlighting the previously proposed relevance of the 400 kyr eccentricity cycle in the EEP for this time period [*Herbert et al.*, 2010]. In contrast, when eccentricity was higher (with an upward increase after 1.85 Ma), Earth's seasonality increased causing greater latitudinal migration of the ITCZ. Thus, the ITCZ may have been located further north, closer to its current position, with a reinforcement of the local winds and decreased rainfalls. This situation would have allowed a higher lithic input, including iron, well sorted around a finer mode. Furthermore, the overall increase in lithic contributions across the studied period, with a greater content from 1.85 Ma, also indicates more arid conditions of the source regions. This enhanced aridity has been also detected in other regions like the African continent during this time period [*deMenocal*, 2004]. Finally, the invariant mineralogical composition along the whole record, including glacial and interglacial phases (Figure S6 and Table S1 in the supporting information), suggests that there were no noticeable changes in the source area of the lithic material in relation to these ITCZ migrations.

In order to better characterize the geographical impact of the discussed ITCZ displacements, ODP Site 1238, located further southeast (1°52.310′S, 82°46.934′W) in the EEP, was also examined for the time period of the most intense LDOs (1.6–1.79 Ma), which occurred during glacial MIS 56. If these events occurred during a weakening of the southeasterly trade winds, it should also be reflected in Site 1238. Thus, the recorded signal in Site 1238 with high fluxes of opal, coarse grains with a similar distribution to cluster E (Figure 6), even with an increased signal due to the shorter transport distance for the lithic material, supports this southward shift of the ITCZ and illustrates the wide geographical extension of the L1.

6.2. Atmosphere-Ocean Coupling

Primary productivity in the EEP is controlled by the availability of nutrient inputs in the system which in turn is influenced by the atmosphere-ocean coupled system. Thus, it is also sensitive to the ITCZ or equatorial front (EF) migration and the associated equatorial upwelling system. Highest values of export production occurred during glacial periods between 1.85 and 2.1 Ma and glacial time located at 1.65 Ma (MIS 56; Figures 5e–5g), when the LDOs were formed. The lithic fraction data (section 6.1) suggest that during these glacial periods, the ITCZ was located over the equator (ODP Site 1240 location) likely at its most southward position over the entire record. The dominance of the cluster E occurred primarily during periods when opal and TOC were high; thus, the interpreted weak trade winds could not stimulate this high-productivity system (Figure 5). In addition, this high productivity could not be explained through an iron fertilization process as could be expected in an iron-limited ocean region [*Martin*, 1990; *Jickells et al.*, 2005], since iron values are relatively
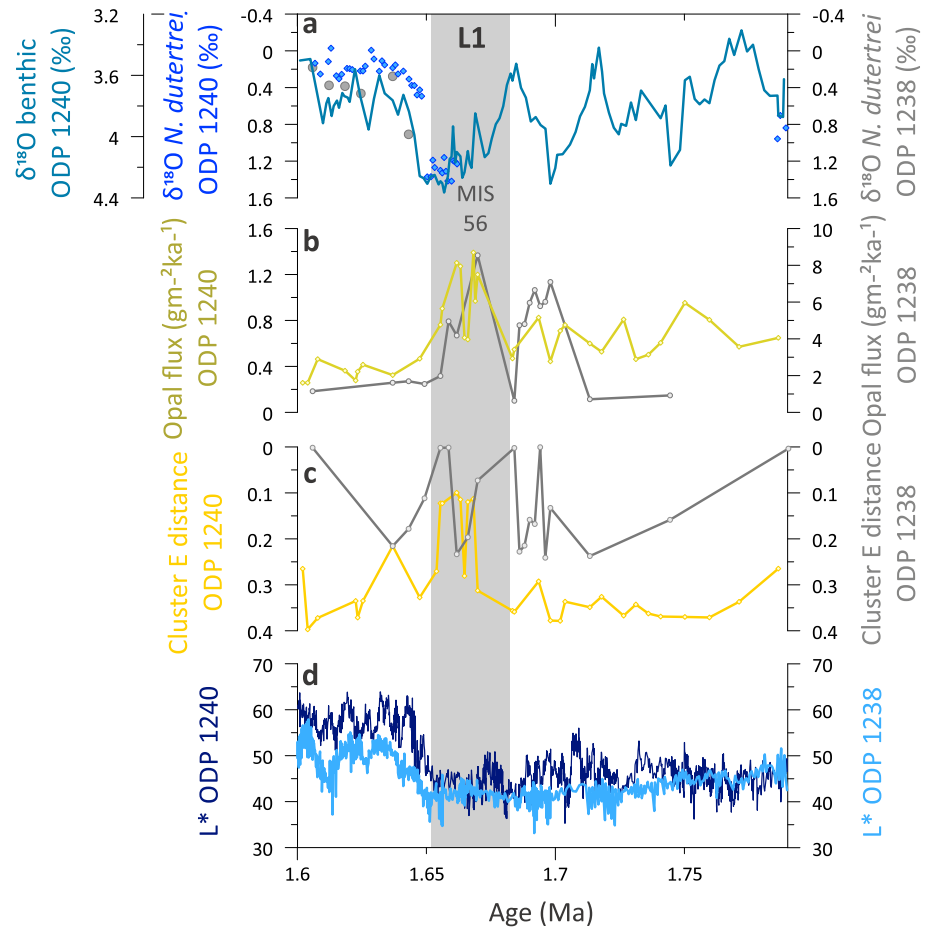
Figure 6. The imprint of a major southward ITCZ migration during L1 (1.6–1.79 Ma), registered further south over ODP Site 1238. (a) ODP Site 1240 benthic $\delta^{18}O$ record ($^0/_{00}$; blue line), ODP Site 1240 *Neogloboquadrina dutertrei* $\delta^{18}O$ record ($^0/_{00}$; blue diamonds), and ODP Site 1238 *N. dutertrei* $\delta^{18}O$ record ($^0/_{00}$; dark gray circles). (b) Opal flux (gm^{-2} ka^{-1}) from ODP Site 1240 (green line) and ODP Site 1238 (dark gray line). (c) Cluster E distance from ODP Site 1240 (yellow line) and ODP Site 1238 (dark gray line). (d) Luminescence (L*) from ODP Site 1240 (dark blue line) and ODP Site 1238 (light blue line) [*Blum et al.*, 2005]. The gray shaded bar shows the locations of L1 and MIS 56.

low before 1.85 Ma. A comparison with a sedimentary $\delta^{15}N$ isotope record from the same marine core [*Etourneau et al.*, 2013] also reveals low $\delta^{15}N$ values specially during this interval prior to 1.85 Ma transition (Figure 5d). *Etourneau et al.* [2013] interpreted this as a reflection of enhanced nitrate availability in the eastern equatorial Pacific system, suggesting that nutrient consumption was low relative to nutrient supply. Thus, the low $\delta^{15}N$ values when export production was high indicate a significant supply of nutrients, including silicic acid and nitrate [*Billups et al.*, 2013], to the eastern equatorial Pacific between 1.85 and 2.1 Ma. Since the EEP is Si and iron colimited [*Brzezinski et al.*, 2008, 2011], diatoms tend to deplete surface waters of silicic acid before nitrate, reducing the Si(OH)$_4$:NO$_3$ ratio in the surface ocean [*Hutchins and Bruland*, 1998]. This major silicic acid uptake promotes more silicified diatoms, with heavier and larger frustules [*Franck et al.*, 2000; *Beucher et al.*, 2007], thus allowing for faster sinking and the formation of the LDOs during these periods prior to 1.85 Ma. The *Thalassiothrix* spp. diatoms, typical of these LDOs, have been associated to the dominance of stratified surface waters in the vicinity of the EF [*Kemp et al.*, 2000, 2006; *Pike and Stickley*, 2007]. The occurrence of these laminations has also been associated to major cooling events in the eastern equatorial Pacific [*Kemp et al.*, 1995]. This seems to be confirmed by excursions toward cooler SST during LDO deposition as evidenced by alkenone-derived SST record (Figure 5b) [*Liu and Herbert*, 2004; *Herbert et al.*, 2010]. This is not true for two laminations (L3 and L8) that record higher SSTs. This may be explained by the seasonality of the coccolithophorid population. The inferred stratified conditions are consistent with the interpreted ITCZ location over equator. But, the stimulated diatom productivity also requires an extra arrival of silicic acid to the EEP, likely through advection of

nutrient-rich intermediate waters feeding the EUC. Previous studies have identified strong connections between high and low latitudes, mainly through advection of Southern Ocean intermediate water to the Equatorial Undercurrent (EUC) [*Kessler*, 2006; *Pena et al.*, 2013]. This Antarctic component would have provided Si-rich waters to the tropical thermocline [*Calvo et al.*, 2011], stimulating diatom production (Figure 5e) and a consequent increase in nitrate availability [*Sarmiento et al.*, 2004]. This high-latitude forcing is confirmed by the strong obliquity signal on the opal record during the interval previous to 1.85 Ma (Figure S8 in the supporting information). Consequently, prior to the 1.85 Ma transition, we interpret that the fertilization of the EEP occurred through an enhanced EUC nutrient supply, potentially of Southern Ocean origin, as also published in *Etourneau et al.* [2013].

After 1.85 Ma, according to the lithic fraction interpretation, the ITCZ changed its mean position toward a more northern location, particularly during glacial times. This situation would have triggered enhanced equatorial upwelling, less stratified surface waters, a thermocline shoaling, and a greater equatorial E-W Pacific gradient (Figure 5c), consistent with the enhancement in Walker circulation proposed in previous studies [*Ravelo et al.*, 2004; *Wara et al.*, 2005; *Ford et al.*, 2012]. The productivity proxies indicate a decrease but still relatively high values in export production (Figures 5e and 5g) and a clear change in the phytoplankton community, supported by a lowering in the Si_{bio}:TOC ratio and the disappearance of the heavy silicified diatoms that formed the LDOs (Figure 5f). This evidence and the parallel increase nitrate consumption (Figure 5d) suggest a change in the $Si(OH)_4$:NO_3 ratio consistent with a reduction in the availability of silicic acid and/or enhanced iron fertilization. The reinforcement of the upwelling system by southeasterly trade winds produced SST slightly lower after 1.85 Ma and also increased the atmospheric dust transport as is supported by the relatively high lithic and iron fluxes (Figures 5j and 5k). The exception to this situation occurred during the glacial MIS 56 (1.65 Ma), when conditions returned to those of glacial previous to 1.85 Ma, but with a more extreme expression. This southward displacement of the ITCZ may be a consequence of the extreme glaciation triggered by 400 kyr minimum eccentricity at 1.65 Ma, as already seen it in numerical models [*Masunaga and L'Ecuyer*, 2011]. The ITCZ displacement reached further south, to the position of Site 1238, confirming the severity of the glacial MIS 56 period. On the other hand, although the most marked and important changes are observed during glacial periods before and after 1.85 Ma, the interglacial phases also show a different pattern of behavior between these two marked periods, such as TOC and opal fluxes (Figures 5e and 5g). These evidence support a tight coupling between the atmospheric changes and the upwelling system and highlight the high dynamism of the equatorial system during the studied period.

6.3. Implications for Carbon Fluxes to the Deep-Sea Floor

The TOC record (Figure 5g) shows the highest fluxes during the period covering lithological subunit 1B (1.65–2.08 Ma), supporting an enhanced C export to the deep ocean. Nevertheless, C fluxes appear to be slightly higher prior to the 1.85 Ma transition and, particularly, during those glacial periods with LDO formation. *Uvigerina* spp. is a detritivore and infaunal benthic foraminifera, typical of environments with a high organic carbon flux and low oxygen content [*Seiglie*, 1968; *Murray*, 1991; *Rathburn and Corliss*, 1994]. In general, *Uvigerina* spp. abundances parallel the TOC variability, with maximum percentages of *Uvigerina* spp. occurring during maxima in TOC. However, this relationship is not satisfied during most of the LDOs (Figures 4a, 4b, and 5g). These time intervals of maximum TOC fluxes toward the deep ocean did not stimulate the proliferation of *Uvigerina* spp., theoretically prone to high carbon fluxes. This very distinctive response of the benthic system to two primary productivity scenarios suggests different mechanisms of carbon sinking to the deep ocean. LDO layers are formed by pennate-type diatoms, such as *Thalassiothrix* spp. [*Mix et al.*, 2003]. These diatoms tend to form large grids of twisted cells, which could drag down large amounts of organic carbon and other particles to the deep-sea floor. These high fluxes of TOC would have occurred in rapid events, probably as seasonal cycles (especially during fall or early winter) [*Kemp et al.*, 2000] rather than as a continuous and homogeneous rain, and apparently prevented the development of *Uvigerina* spp. owing to the extremely high contents of TOC. These results highlight the role of vertical particle transport controlling the benthic population and also document the high efficiency of the LDOs in the deep transfer and storage of carbon and their potential to increase the storage of atmospheric CO_2 in the deep ocean [*Dugdale and Wilkerson*, 2001; *Kemp et al.*, 2000, 2006].

7. Conclusions

The integrated study of both lithic and biogenic components from EEP sediments allows the identification of coupled changes in atmospheric and oceanic dynamics that occurred along the early Pleistocene (from 1.56 to 2.26 Ma) indicating major meridional shifts in the main position of the ITCZ.

Glacial periods from 1.85 to 2.26 Ma present lower iron and lithic contents, dominated by coarse and unsorted lithic particles, interpreted to reflect a southerly position of the ITCZ, approximately over the equator (ODP Site 1240). This would result in a weakening of the trade winds over the region and increasing wet dust deposition associated with more frequent rainfall events below the ITCZ. This situation is consistent with the dominance of the heavy silicified diatom that formed the LDOs, typical of stratified surface waters in the vicinity of oceanic frontal zones. The increased N availability (low $\delta^{15}N$ values) [*Etourneau et al.*, 2013] and opal fluxes, particularly after 2.1 Ma, support a change in the nutrient availability likely induced by a greater input of silicic acid-rich waters, potentially from Antarctic origin. The high-latitude origin of these Si-rich waters is supported by the detected obliquity pacing in the biological Si record. The almost absence of *Uvigerina* spp., a benthic species that usually takes advantage of high TOC fluxes, supports a high and rapid flux of carbon toward the deep ocean that overwhelmed the benthic ecosystem during LDO formation.

Glacial periods after 1.85 Ma present higher deposition of finer and better sorted lithic particles and also enhanced iron fluxes. These conditions could reflect the dominance of eolian dry deposition as a result of a northward migration of the ITCZ. This interpretation is supported by the evidence of high primary productivity but with remarkable differences in the nutrient balance (less N availability) consistent with conditions of enhanced upwelling and iron fertilization in the region. This situation would have enhanced the E-W gradient in the equatorial Pacific in agreement with the previously proposed strengthening of the Walker circulation after 1.85 Ma. The high resolution of the new ODP Site 1240 records at this time frame has allowed to characterize an abrupt shift in the system located at 1.85 Ma rather than a progressive and smooth long trend change. During this time, carbon flux toward the deep ocean was also high but occurred as a more homogeneous rain that efficiently stimulated the development of *Uvigerina* spp.

The glacial period centered at 1.65 Ma (MIS 56) was an exception to this 1.85 Ma boundary and became a major breakdown to this northward shift of the ITCZ. MIS 56 and also MIS 78 are characterized by the best developed LDOs and also the coldest glacial phases coincident with eccentricity minima paced by the 400 kyr cycle. The seasonal changes derived from this distinctive astronomical configuration combined with the growing ice of the North Hemisphere ice sheets are suggested to have lead the recorded migrations in the ITCZ position.

References

Backman, J., and N. J. Shackleton (1983), Quantitative biochronology of Pliocene and early Pleistocene calcareous nannofossils from the Atlantic, Indian and Pacific Oceans, *Mar. Micropaleontol.*, *8*(2), 141–170.

Behrenfeld, M., and P. G. Falkowski (1997), A consumer's guide to phytoplankton primary productivity models, *Limnol. Oceanogr.*, *42*(7), 1479–1491, doi:10.4319/lo.1997.42.7.1479.

Berger, W. H., T. Bickert, H. Schmidt, G. Wefer, and M. Yasuda (1993), Quaternary oxygen isotope record of pelagic foraminifers: Site 805, Ontong Java Plateau, *Proc. Ocean Drill. Program Sci. Results*, *130*, 363–379.

Betzer, P. R., et al. (1988), Long-range transport of giant mineral aerosol particles, *Nature*, *336*, 568–571.

Beucher, C. P., M. A. Brzezinski, and X. Crosta (2007), Silicic acid dynamics in the glacial sub-Antarctic: Implications for the silicic acid leakage hypothesis, *Global Biogeochem. Cycles*, *21*, GB3015, doi:10.1029/2006GB002746.

Billups, K., A. Aufdenkampe, and R. Hays (2013), Late Miocene through early Pleistocene nutrient utilization and export production in the Antarctic zone of the Southern Ocean, *Global Planet. Change*, *100*, 353–361, doi:10.1016/j.gloplacha.2012.11.014.

Blum, P., A. C. Mix, R. Tiedemann, and Ralf; Shipboard Scientific Party (2005), Color reflectance of ODP Hole 202-1240B, doi:10.1594/ PANGAEA.253486.

Broccoli, A. J., K. A. Dahl, and R. J. Stouffer (2006), Response of the ITCZ to Northern Hemisphere cooling, *Geophys. Res. Lett.*, *33*, L01702, doi:10.1029/2005GL024546.

Brzezinski, M. A., C. Dumousseaud, J. W. Krause, C. I. Measures, and D. M. Nelson (2008), Iron and silicic acid concentrations together regulate Si uptake in the equatorial Pacific Ocean, *Limnol. Oceanogr.*, *53*(3), 875–889, doi:10.4319/lo.2008.53.3.0875.

Brzezinski, M. A., et al. (2011), Co-limitation of diatoms by iron and silicic acid in the equatorial Pacific, *Deep Sea Res., Part II*, *58*(3–4), 493–511, doi:10.1016/j.dsr2.2010.08.005.

Calvo, E., C. Pelejero, L. D. Pena, I. Cacho, and G. A. Logan (2011), Eastern equatorial Pacific productivity and related-CO_2 changes since the last glacial period, *Proc. Natl. Acad. Sci. U.S.A.*, *108*(14), 5537–5541, doi:10.1073/pnas.1009761108.

Cannariato, K. G., and A. C. Ravelo (1997), Pliocene-Pleistocene evolution of eastern tropical Pacific surface water circulation and thermocline depth, *Paleoceanography*, *12*(6), 805, doi:10.1029/97PA02514.

Chelton, D. B., S. K. Esbensen, M. G. Schlax, N. Thum, M. H. Freilich, F. J. Wentz, C. L. Gentemann, M. J. McPhaden, and P. S. Schopf (2001), Observations of coupling between surface wind stress and sea surface temperature in the eastern tropical Pacific, *J. Clim.*, *14*, 1479–1498, doi:10.1175/1520-0442(2001)014<1479:OOCBSW>2.0.CO;2.

Chiang, J. C. H., and C. M. Bitz (2005), Influence of high latitude ice cover on the marine Intertropical Convergence Zone, *Clim. Dyn.*, *25*(5), 477–496, doi:10.1007/s00382-005-0040-5.

Chuey, J. M., D. K. Rea, and N. G. Pisias (1987), Late Pleistocene paleoclimatology of the central equatorial Pacific: A quantitative record of eolian and carbonate deposition, *Quat. Res.*, *28*(3), 323–339.

De Szoeke, S. P., S. P. Xie, T. Miyama, K. J. Richards, and R. J. O. Small (2007), What maintains the SST front north of the eastern Pacific equatorial cold tongue?, *J. Clim.*, *20*(11), 2500–2514, doi:10.1175/JCLI4173.1.

Dekens, P. S., A. C. Ravelo, and M. D. McCarthy (2007), Warm upwelling regions in the Pliocene warm period, *Paleoceanography*, *22*, PA3211, doi:10.1029/2006PA001394.

deMenocal, P. B. (1995), Plio-Pleistocene African climate, *Science*, *270*(5233), 53–59.

deMenocal, P. B. (2004), African climate change and faunal evolution during the Pliocene–Pleistocene, *Earth Planet. Sci. Lett.*, *220*(1–2), 3–24, doi:10.1016/S0012-821X(04)00003-2.

Dugdale, R. C., and F. P. Wilkerson (2001), Sources and fates of silicon in the ocean: The role of diatoms in the climate and glacial cycles, *Sci. Mar.*, *65*, 141–152.

Etourneau, J., P. Martinez, T. Blanz, and R. Schneider (2009), Pliocene–Pleistocene variability of upwelling activity, productivity, and nutrient cycling in the Benguela region, *Geology*, *10*, 871–874, doi:10.1130/G25733A.1.

Etourneau, J., R. Schneider, T. Blanz, and P. Martinez (2010), Intensification of the Walker and Hadley atmospheric circulations during the Pliocene–Pleistocene climate transition, *Earth Planet. Sci. Lett.*, *297*, 103–110, doi:10.1016/j.epsl.2010.06.010.

Etourneau, J., R. S. Robinson, P. Martinez, and R. Schneider (2013), Equatorial Pacific peak in biological production regulated by nutrient and upwelling during the late Pliocene/early Pleistocene cooling, *Biogeosciences*, *10*, 5663–5670, doi:10.5194/bg-10-5663-2013.

Fabres, J., A. Calafat, A. Sanchez-Vidal, M. Canals, and S. Heussner (2002), Composition and spatio-temporal variability of particle fluxes in the Western Alboran Gyre, Mediterranean Sea, *J. Mar. Syst.*, *33–34*, 431–456.

Feakins, S. J., P. B. deMenocal, and T. I. Eglinton (2005), Biomarker records of late Neogene changes in northeast African vegetation, *Geology*, *33*(12), 977–980, doi:10.1130/G21814.1.

Ford, H. L., A. C. Ravelo, and S. Hovan (2012), A deep eastern equatorial Pacific thermocline during the early Pliocene warm period, *Earth Planet. Sci. Lett.*, *355–356*, 152–161, doi:10.1016/j.epsl.2012.08.027.

Franck, V. M., M. A. Brzezinski, K. H. Coale, and D. M. Nelson (2000), Iron and silicic acid concentrations regulate Si uptake north and south of the Polar Frontal Zone in the Pacific sector of the Southern Ocean, *Deep Sea Res., Part II*, *47*, 3315–3338.

Glaccum, R. A., and J. M. Prospero (1980), Saharan aerosols over the tropical North Atlantic—Mineralogy, *Mar. Geol.*, *37*(3–4), 295–321.

Guerzoni, S., E. Molinaroli, and R. Chester (1997), Saharan dust inputs to the western Mediterranean Sea: Depositional patterns, geochemistry and sedimentological implications, *Deep Sea Res., Part II*, *44*(3–4), 631–654.

Hartley, A. J., and G. Chong (2002), Late Pliocene age for the Atacama Desert: Implications for the desertification of western South America, *Geology*, *30*(1), 43–46.

Hastie, T., R. Tibshirani, and J. Friedman (2001), *Elements of Statistical Learning*, Springer, Stanford, Calif.

Herbert, T. D., L. C. Peterson, K. T. Lawrence, and Z. Liu (2010), Tropical ocean temperatures over the past 3.5 million years, *Science*, *328*(5985), 1530–4, doi:10.1126/science.1185435.

Hovan, S. A. (1995), Late Cenozoic atmospheric circulation intensity and climatic history recorded by eolian deposition in the eastern equatorial Pacific Ocean, Leg 138, *Proc. Ocean Drill. Program Sci. Results*, *138*, 615–625.

Hutchins, D. A., and K. W. Bruland (1998), Iron-limited diatom growth and Si:N uptake ratios in a coastal upwelling regime, *Nature*, *393*, 561–564, doi:10.1038/31203.

Hyeong, K., C. M. Yoo, J. Kim, S. B. Chi, and K. H. Kim (2006), Flux and grain size variation of eolian dust as a proxy tool for the paleo-position of the Intertropical Convergence Zone in the northeast Pacific, *Palaeogeogr. Palaeoclimatol. Palaeoecol.*, *241*(2), 214–223, doi:10.1016/j.palaeo.2006.03.011.

Janecek, T., and D. K. Rea (1985), Quaternary fluctuations in the Northern Hemisphere trade winds and westerlies, *Quat. Res.*, *24*(2), 150–163.

Jansen, E., L. A. Mayer, J. Backman, R. M. Leckie, and T. Takayama (1993), Evolution of Pliocene climate cyclicity at Hole 806B (5–2 Ma): Oxygen isotope record, *Proc. Ocean Drill. Program Sci. Results*, *130*, 349–362.

Jansen, J. H. F., S. J. Van Der Gaast, B. Koster, and A. J. Vaars (1998), Short communication CORTEX, a shipboard XRF-scanner for element analyses in split sediment cores, *Mar. Geol.*, *151*, 143–153.

Jeong, G. Y., J. Y. Kim, J. Seo, G. M. Kim, H. C. Jin, and Y. Chun (2013), Long-range transport of giant particles in Asian dust identified by physical, mineralogical, and meteorological analysis, *Atmos. Chem. Phys. Discuss.*, *13*(8), 21,041–21,077, doi:10.5194/acpd-13-21041-2013.

Jickells, T. D., et al. (2005), Global iron connections between desert dust, ocean biogeochemistry, and climate, *Science*, *308*(5718), 67–71, doi:10.1126/science.1105959.

Karnauskas, K. B., R. Murtugudde, and A. J. Busalacchi (2007), The effect of the Galápagos Islands on the equatorial Pacific cold tongue, *J. Phys. Oceanogr.*, *37*(5), 1266–1281, doi:10.1175/JPO3048.1.

Karnauskas, K. B., R. Murtugudde, and A. J. Busalacchi (2010), Observing the Galápagos–EUC interaction: Insights and challenges, *J. Phys. Oceanogr.*, *40*(12), 2768–2777, doi:10.1175/2010JPO4461.1.

Kaupp, L. J., C. I. Measures, K. E. Selph, and F. T. Mackenzie (2011), The distribution of dissolved Fe and Al in the upper waters of the eastern equatorial Pacific, *Deep Sea Res., Part II*, *58*(3–4), 296–310, doi:10.1016/j.dsr2.2010.08.009.

Kemp, A. E. S., J. Baldauf, and R. Pearce (1995), Origins and paleoceanographic significance of laminated diatom ooze from the eastern equatorial Pacific Ocean, *Proc. Ocean Drill. Program Sci. Results*, *138*, 641–645.

Kemp, A. E. S., J. Pike, R. B. Pearce, and C. B. Lange (2000), The "fall dump"—A new perspective on the role of a "shade flora" in the annual cycle of diatom production and export flux, *Deep Sea Res., Part II*, *47*, 2129–2154.

Kemp, A. E. S., R. B. Pearce, I. Grigorov, J. Rance, C. B. Lange, P. Quilty, and I. Salter (2006), Production of giant marine diatoms and their export at oceanic frontal zones: Implications for Si and C flux from stratified oceans, *Global Biogeochem. Cycles*, *20*, GB4S04, doi:10.1029/2006GB002698.

Kessler, W. S. (2006), The circulation of the eastern tropical Pacific: A review, *Prog. Oceanogr.*, *69*(2–4), 181–217, doi:10.1016/j.pocean.2006.03.009.

Koutavas, A., and J. Lynch-Stieglitz (2004), Variability of the marine ITCZ over the eastern Pacific during the past 30,000 years, *Reg. Perspect. Glob. Context*, 1–26.

Laskar, J., P. Robutel, F. Joutel, M. Gastineau, A. C. M. Correia, and B. Levrard (2004), A long-term numerical solution for the insolation quantities of the Earth, *Astron. Astrophys.*, *428*(1), 261–285, doi:10.1051/0004-6361:20041335.

Lawrence, K. T., Z. Liu, and T. Herbert (2006), Evolution of the eastern tropical Pacific through Plio-Pleistocene glaciation, *Science*, *312*(5770), 79–83, doi:10.1126/science.1120395.

Lisiecki, L. E., and M. E. Raymo (2005), A Pliocene-Pleistocene stack of 57 globally distributed benthic δ^{18}O records, *Paleoceanography*, *20*, PA1003, doi:10.1029/2004PA001071.

Liu, Z., and T. D. Herbert (2004), High-latitude influence on the eastern equatorial Pacific climate in the early Pleistocene epoch, *Nature*, *427*, 720–723, doi:10.1038/nature02295.1.

Liu, Z., M. A. Altabet, and T. D. Herbert (2008), Plio-Pleistocene denitrification in the eastern tropical North Pacific: Intensification at 2.1 Ma, *Geochem. Geophys. Geosyst.*, *9*, Q11006, doi:10.1029/2008GC002044.

Lyle, M., D. W. Murray, B. P. Finney, J. Dymond, J. M. Robbins, and K. Brooksforce (1988), The record of late Pleistocene biogenic sedimentation in the eastern tropical Pacific Ocean, *Paleoceanography*, *3*(1), 39–59, doi:10.1029/PA003i001p00039.

Ma, Z., A. C. Ravelo, Z. Liu, L. Zhou, and A. Paytan (2015), Export production fluctuations in the eastern equatorial Pacific during the Pliocene-Pleistocene: Reconstruction using barite accumulation rate, *Paleoceanography*, *30*, 1455–1469, doi:10.1002/2015PA002860.

Mahowald, N. M., A. R. Baker, G. Bergametti, N. Brooks, R. A. Duce, T. D. Jickells, N. Kubilay, J. M. Prospero, and I. Tegen (2005), Atmospheric global dust cycle and iron inputs to the ocean, *Global Biogeochem. Cycles*, *19*, GB4025, doi:10.1029/2004GB002402.

Marlow, J. R., C. B. Lange, G. Wefer, and A. Rosell-mele (2000), Upwelling intensification as part of the Pliocene-Pleistocene climate transition, *Science*, *290*, 2288–2292.

Marshall, J., A. Donohoe, D. Ferreira, and D. McGee (2014), The ocean's role in setting the mean position of the Inter-Tropical Convergence Zone, *Clim. Dyn.*, *42*(7–8), 1967–1979, doi:10.1007/s00382-013-1767-z.

Martin, J. H. (1990), Glacial-interglacial CO_2 change: The iron hypothesis, *Paleoceanography*, *5*(1), 1–13, doi:10.1029/PA005I001P00001.

Masunaga, H., and T. S. L'Ecuyer (2011), Equatorial asymmetry of the east Pacific ITCZ: Observational constraints on the underlying processes, *J. Clim.*, *24*(6), 1784–1800, doi:10.1175/2010JCLI3854.1.

McGee, D., A. Donohoe, J. Marshall, and D. Ferreira (2014), Changes in ITCZ location and cross-equatorial heat transport at the Last Glacial Maximum, Heinrich Stadial 1, and the mid-Holocene, *Earth Planet. Sci. Lett.*, *390*, 69–79, doi:10.1016/j.epsl.2013.12.043.

Mix, A. C., et al. (2003), Leg 202 summary, *Proc. ODP, Init. Repts., 202: College Station*, Tex (Ocean Drilling Program), doi:10.2973/odp.proc.ir.202.2003.

Molina-Cruz, A. (1977), The relation of the southern trade winds to upwelling processes during the last 75,000 years, *Quat. Res.*, *8*(3), 324–338.

Moreno, A., J. Targarona, J. Henderiks, M. Canals, T. Freudenthal, and H. Meggers (2001), Orbital forcing of dust supply to the North Canary Basin over the last 250 kyr, *Quat. Sci. Rev.*, *20*, 1327–1339.

Mortlock, R. A., and P. N. Froelich (1989), A simple method for the rapid determination of biogenic opal in pelagic marine sediments, *Deep Sea Res., Part A*, *36*(9), 1415–1426, doi:10.1016/0198-0149(89)90092-7.

Murray, J. W. (1991), *Ecology and Palaeoecology of Benthic Foraminifera*, Longman Group UK limited, London.

Murray, R. W., M. Leinen, A. C. Mix, and C. H. Polsky (2000), Export production and carbonate dissolution in the central equatorial Pacific Ocean over the past 1 Myr, *Paleoceanography*, *15*(6), 570–592, doi:10.1029/1999PA000457.

Nakai, S., A. N. Halliday, and D. K. Rea (1993), Provenance of dust in the Pacific Ocean, *Earth Planet. Sci. Lett.*, *119*, 143–157.

O'Brien, C. L., G. L. Foster, M. A. Martínez-Botí, R. Abell, J. W. B. Rae, and R. D. Pancost (2014), High sea surface temperatures in tropical warm pools during the Pliocene, *Nat. Geosci.*, *7*(8), 606–611, doi:10.1038/ngeo2194.

Pak, H., and J. Zaneveld (1974), Equatorial front in the eastern Pacific Ocean, *J. Phys. Oceanogr.*, *4*, 570–578.

Pena, L. D., S. L. Goldstein, S. R. Hemming, K. M. Jones, E. Calvo, C. Pelejero, and I. Cacho (2013), Rapid changes in meridional advection of Southern Ocean intermediate waters to the tropical Pacific during the last 30 kyr, *Earth Planet. Sci. Lett.*, *368*, 20–32, doi:10.1016/j.epsl.2013.02.028.

Peterson, L. C., and G. H. Haug (2006), Variability in the mean latitude of the Atlantic Intertropical Convergence Zone as recorded by riverine input of sediments to the Cariaco Basin (Venezuela), *Palaeogeogr. Palaeoclimatol. Palaeoecol.*, *234*, 97–113, doi:10.1016/j.palaeo.2005.10.021.

Pike, J., and C. E. Stickley (2007), Diatom records: Marine laminated sequences, in *Encyclopedia of Quaternary Science*, edited by S. A. Elias, pp. 557–567, Elsevier, Amsterdam, doi:10.1016/B0-44-452747-8/00238-6.

Povea, P., I. Cacho, A. Moreno, M. Menéndez, and F. J. Méndez (2015), A new procedure for the lithic fraction characterization in marine sediments from high productivity areas: Optimization of analytical and statistical procedures, *Limnol. Oceanogr. Methods*, *13*(3), 127–137, doi:10.1002/lom3.10013.

Pye, K. (1995), The nature, origin and accumulation of loess, *Quat. Sci. Rev.*, *14*, 653–667.

Rathburn, A. E., and B. H. Corliss (1994), The ecology of living (stained) deep-sea benthic foraminifera from the Sulu Sea, *Paleoceanography*, *9*(1), 87–150, doi:10.1029/93PA02327.

Ravelo, A. C., D. H. Andreasen, M. Lyle, A. Olivarez Lyle, and M. W. Wara (2004), Regional climate shifts caused by gradual global cooling in the Pliocene epoch, *Nature*, *429*(6989), 263–267, doi:10.1038/nature02567.

Ravelo, A. C., K. T. Lawrence, A. Fedorov, and H. L. Ford (2014), Comment on "A 12-million-year temperature history of the tropical Pacific Ocean", *Science*, *346*(6216), doi:10.1126/science.1257618.

Rea, D. K. (1990), Aspects of atmospheric circulation: The Late Pleistocene (0–950,000 yr) record of eolian deposition in the Pacific Ocean, *Palaeogeogr. Palaeoclimatol. Palaeoecol.*, *78*, 217–227.

Richter, T. O., S. van der Gaast, B. Koster, A. Vaars, R. Gieles, H. C. de Stigter, H. De Haas, and T. C. E. van Weering (2006), The Avaatech XRF core scanner: Technical description and applications to NE Atlantic sediments, *Geol. Soc. Lond. Spec. Publ.*, *267*(1), 39–50, doi:10.1144/GSL.SP.2006.267.01.03.

Röhl, U., and L. J. Abrams (2000), High-resolution, downhole, and nondestructive core measurements from Sites 999 and 1001 in the Caribbean Sea: Application to the late Paleocene thermal maximum, in *Proceedings of the ODP*, *Sci. Results*, vol. 165, edited by R. M. Leckie et al., pp. 191–203, Ocean Drilling Program, College Station, Tex.

Rothwell, R. (1989), *Minerals and Mineraloids in Marine Sediments: An Optical Identification Guide*, vol. 166, Springer, Netherlands.

Sachs, J. P., D. Sachse, R. H. Smittenberg, Z. Zhang, D. S. Battisti, and S. Golubic (2009), Southward movement of the Pacific Intertropical Convergence Zone AD 1400–1850, *Nat. Geosci.*, *2*(7), 519–525, doi:10.1038/ngeo554.

Sáez, A., L. Cabrera, M. Garcés, P. Van Den Bogaard, A. Jensen, and D. Gimeno (2012), The stratigraphic record of changing hyperaridity in the Atacama desert over the last 10 Ma, *Earth Planet. Sci. Lett.*, *355–356*, 32–38, doi:10.1016/j.epsl.2012.08.029.

Sarmiento, J. L., N. Gruber, M. A. Brzezinski, and J. P. Dunne (2004), High-latitude controls of thermocline nutrients and low latitude biological productivity, *Nature*, *427*, doi:10.1038/nature02204.1.

Schneider, T., T. Bischoff, and G. H. Haug (2014), Migrations and dynamics of the Intertropical Convergence Zone, *Nature*, *513*(7516), 45–53, doi:10.1038/nature13636.

Seiglie, G. A. (1968), Foraminiferal assemblages as indicators of high organic carbon content in sediments and of polluted waters, *Am. Assoc. Pet. Geol. Bull.*, *52*(11), 2231–2241.

Shackleton, N. J., and M. A. Hall (1984), Oxygen and carbon isotope stratigraphy of Deep Sea Drilling Project hole 552A: Plio-Pleistocene glacial history, *Initial Rep. Deep Sea Drill. Proj.*, *81*, 599–609.

Tegen, I., A. L. Lacis, and I. Fung (1996), The influence on climate forcing of mineral aerosols from disturbed soils, *Nature*, *380*, 419–422, doi:10.1038/380419a0.

Terry, R. D., and G. V. Chilingar (1955), *Comparison Charts for Visual Estimation of Percent Composition*, Allen Hancock Foundation, Los Angeles, Calif. Reprinted from *J. Sed. Petrology*, *23*, 226-234.

Trauth, M. H., M. A. Maslin, A. L. Deino, M. R. Strecker, A. G. N. Bergner, and M. Dühnforth (2007), High- and low-latitude forcing of Plio-Pleistocene East African climate and human evolution, *J. Hum. Evol.*, *53*(5), 475–486, doi:10.1016/j.jhevol.2006.12.009.

Wara, M. W., A. C. Ravelo, and M. L. Delaney (2005), Permanent El Niño-like conditions during the Pliocene warm period, *Science*, *309*(5735), 758–761, doi:10.1126/science.1112596.

Weber, M. E., and N. G. Pisias (1999), Spatial and temporal distribution of biogenic carbonate and opal in deep-sea sediments from the eastern equatorial Pacific: Implications for ocean history since 1.3 Ma, *Earth Planet. Sci. Lett.*, *174*, 59–73.

Windom, H. L. (1985), Eolian contributions to marine sediments, *J. Sediment. Petrol.*, *45*, 520–529.

Wyrtki, K. (1967), Circulation and water masses in the eastern equatorial Pacific Ocean, *Int. J. Oceanol. Limnol.*, *1*(2), 117–147.

Wyrtki, K. (1974), Equatorial currents in the Pacific 1950–1970 and their relations to trade winds, *J. Phys. Oceanogr.*, *4*, 372–380.

Wyrtki, K. (1981), An estimate of equatorial upwelling in the Pacific, *J. Phys. Oceanogr.*, *11*, 1205–1214.

Xie, S. P., and G. H. Philander (1994), A coupled ocean-atmosphere model of relevance to the ITCZ in the eastern Pacific, *Tellus*, *46A*, 340–350.

Zhang, Y. G., M. Pagani, and Z. Liu (2014), A 12-million-year temperature history of the tropical Pacific Ocean, *Science*, *344*(6179), 84–7, doi:10.1126/science.1246172.